

# Three-Dimensional Simulations of Deep-Water Breaking Waves

Kyle A. Brucker<sup>1</sup>, Thomas T. O'Shea<sup>1</sup>, Douglas G. Dommermuth<sup>1</sup>, and Paul Adams<sup>2</sup>

<sup>1</sup>Naval Hydrodynamics Division, Science Applications International Corporation,  
10260 Campus Point Drive, MS 34, San Diego, CA 92121

<sup>2</sup>Unclassified Data Analysis and Assessment Center,  
U.S. Army Engineering Research and Development Center, MS 39180

## Abstract

The formulation of a canonical deep-water breaking wave problem is introduced, and the results of a set of three-dimensional numerical simulations for deep-water breaking waves are presented. In this paper fully nonlinear progressive waves are generated by applying a normal stress to the free surface. Precise control of the forcing allows for a systematic study of four types of deep-water breaking waves, characterized herein as weak plunging, plunging, strong plunging, and very strong plunging.

The three-dimensional iso contours of vorticity exhibit intense streamwise vorticity shortly after the initial ovular cavity of air is entrained during the primary plunging event. An array of high resolution images are presented as a means to visually compare and contrast the major events in the breaking cycles of each case. The volume-integrated energy shows 50% or more of the peak energy is dissipated in strong and very strong plunging events. The volume of air entrained beneath the free surface is quantified. For breaking events characterized by plunging, strong plunging and very strong plunging, significant quantities of air remain beneath the free surface long after the initial breaking event. The rate at which the air beneath the free surface degasses is linear and the same in all cases. The use of volume-weighted (Reynolds) and mass-weighted (Favre) averages are compared, and it is found that statistics obtained by Favre averaging show better agreement with respect to the position of free surface than do those obtained by Reynolds averaging. The average volume fraction plotted on a log scale is used to visually elucidate small volumes of air entrained below the free surface. For the strong plunging and very strong plunging cases significant air is also entrained after the initial plunging event at the toe of spilling breaking region. Improvements to the Numerical Flow Analysis code, which expand the types of problems it can accurately simulate are discussed, along with the results of a feasibility study which shows that simulations with 5-10 billion unknowns are

now tractable.

## Introduction

Surface wave breaking in deep water plays an important role in many engineering and geophysical problems. The interested reader is referred to review articles by [Melville \(1996\)](#) and [Duncan \(2001\)](#) and the detailed discussion of deep-water breaking waves in [Rapp and Melville \(1990\)](#). The focus here remains on aspects relevant to the numerical simulation of breaking waves.

Historically, the two main types of simulations to simulate free-surface flows are the boundary integral equations method (BIEM) and high-order spectral (HOS) methods. These calculations fail at the point at which the surface impacts upon itself, if not sooner. They also employ a single-phase approximation in which the effects of the air on the water are neglected.

Here, we advance the numerical study of breaking waves by introducing a numerical method to simulate three-dimensional, non-linear deep-water breaking waves, and a consistent statistical framework in which to analyze the results. The following framework is introduced for studying a canonical deep-water breaking wave. Consider a single wave, with wavenumber  $k$ , which is propagating as part of a train of waves in deep-water. The computational domain, shown in [Figure 1](#), moves with the linear crest speed of the wave, and is periodic in the stream-wise,  $x$ , direction. The temporally evolving frame-work is conceptually similar to the frame-work employed to simulate fully-developed turbulent channel flow by [Moin and Kim \(1982\)](#), plain mixing layers by [Rogers and Moser \(1994\)](#), and plane wakes by [Moser et al. \(1998\)](#).

The organization of the paper is as follows: First, the theoretical frame work for studying a canonical breaking wave is developed. Second, a method to generate non-linear progressive waves and its validation are discussed, along with the other computational details specific to simulating breaking waves. Third, the results of a

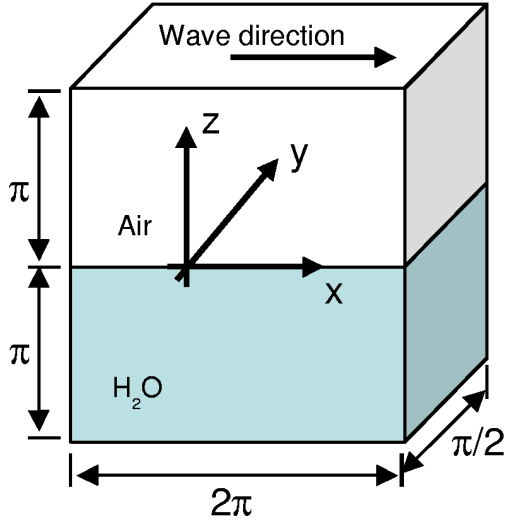


**Figure 1:** Schematic of computational domain.

parametric study of deep-water plunging breaking events are discussed. This discussion is split into three sections, (1) Three-dimensional flow visualization, (2) Integrated energetics and the quantification of air entrainment, (3) Statistical decomposition of the energy into kinetic, turbulent kinetic and potential energy modes. Prior to the conclusions, the results of a feasibility study on simulations with 5-10 billion unknowns are discussed.

## Numerical Method

Four types of wave breaking are studied. For the sake of discussion herein they are defined as weak plunging (WP), plunging (P), strong plunging (SP), and very strong plunging (VSP).

Physical quantities are normalized by characteristic velocity ( $U_o$ ), length ( $L_o$ ), time ( $L_o/U_o$ ), water density ( $\rho_w$ ), and pressure ( $\rho_w U_o^2$ ) scales. Consider the turbulent flow at the interface between air and water with  $\rho_a$  and  $\rho_w$  respectively denoting the densities of air and water

Let  $\alpha$  denote the volume fraction of fluid that is inside a cell. By definition,  $\alpha = 0$  for a cell that is totally filled with air, and  $\alpha = 1$  for a cell that is totally filled with water. In terms of  $\alpha$ , the normalized density is expressed as

$$\rho(\alpha) = \gamma + (1 - \gamma)\alpha, \quad (1)$$

where  $\gamma = \rho_a/\rho_w$  is the density ratio between air and water. Let  $u_i$  denote the normalized three-dimensional velocity field as a function of normalized space ( $x_i$ ) and normalized time ( $t$ ). The conservation of mass is

$$\frac{\partial \rho}{\partial t} + \frac{\partial u_j \rho}{\partial x_j} = 0. \quad (2)$$

For incompressible flow,

$$\frac{\partial \rho}{\partial t} + u_j \frac{\partial \rho}{\partial x_j} = 0. \quad (3)$$

Subtracting Equation (3) from (2) gives a solenoidal condition for the velocity:

$$\frac{\partial u_i}{\partial x_i} = 0. \quad (4)$$

Substituting Equation (1) into (2) and making use of (4), provides an advection equation for the volume fraction:

$$\frac{\partial \alpha}{\partial t} + \frac{\partial}{\partial x_j} (u_j \alpha) = 0. \quad (5)$$

For an infinite Reynolds number, viscous stresses are negligible, and the conservation of momentum is

$$\frac{\partial u_i}{\partial t} + \frac{\partial}{\partial x_j} (u_j u_i) = -\frac{1}{\rho} \frac{\partial p}{\partial x_i} - \frac{p_s}{\rho} \frac{\partial H(\alpha)}{\partial x_i} - \frac{\delta_{i3}}{F_r^2}, \quad (6)$$

where  $F_r^2 = U_o^2/(gL_o)$  is the Froude number, and  $g$  is the acceleration of gravity.  $p$  is the pressure and  $p_s$  is a stress that acts normal to the interface.  $H(\alpha)$  is a Heaviside function, and  $\delta_{ij}$  is the Kronecker delta function.

The divergence of the momentum equations (6) in combination with the solenoidal condition (4) provides a Poisson equation for the dynamic pressure:

$$\frac{\partial}{\partial x_i} \frac{1}{\rho} \frac{\partial p}{\partial x_i} = \Sigma, \quad (7)$$

where  $\Sigma$  is a source term. The pressure is used to project the velocity onto a solenoidal field. Details of the volume fraction advection, the pressure projection, and the numerical time integration are provided in Dommermuth et al. (2007) and O'Shea et al. (2008). Sub-grid scale stresses are modeled using an implicit model that is built into the treatment of convective terms. The performance of the implicit SGS model is provided in Rottman et al. (2010). Specific issues relevant to the current study include free-surface smoothing and interfacial forcing, and are discussed in the next sections.

## SMOOTHING

The free-surface boundary layer is not resolved in volume of fluid (VOF) simulations at high Reynolds numbers with large density jumps such as air and water. Under these circumstances, the tangential velocity is discontinuous across the free-surface interface and the normal component is continuous. As a result, unphysical tearing of the free surface tends to occur. Favre-like filtering can be used to alleviate this problem by forcing the air velocity slightly above the interface to be driven

by the water velocity slightly below the interface in a physical manner. Consider the following filter,

$$u_i^* = \frac{\overline{\rho u_i}}{\bar{\rho}} \text{ for } \alpha \geq 0.5, \quad (8)$$

where  $u_i^*$  is the smoothed velocity field,  $u_i$  is the unfiltered velocity field,  $\rho$  is the density, and  $\alpha$  is the volume fraction. Overline symbols denote averaging over a small control volume.

$$\overline{F(x)} = \int_V W(\xi) F(x - \xi) dV. \quad (9)$$

Here,  $F(x)$  is a general function,  $v$  is a control volume that surrounds a cell, and  $W(x)$  is a weighting function that neither overshoots or undershoots the maximum or minimum allowable density. Due to the high density ratio between water and air, Equation (8) tends to push the water-particle velocity into the air. Once the velocity is filtered, we need to project it back onto a solenoidal field in the fluid volume (V):

$$u_i = u_i^* - \frac{1}{\rho} \frac{\partial \phi}{\partial x_i} \text{ in } V, \quad (10)$$

where  $\phi$  is a potential function. For an incompressible flow, we require that  $u_i$  is solenoidal care of Equation (4). Substituting (10) into (4) gives a Poisson equation for  $\phi$ :

$$\frac{\partial}{\partial x_i} \frac{1}{\rho} \frac{\partial \phi}{\partial x_i} = \frac{\partial u_i^*}{\partial x_i} \text{ in } V. \quad (11)$$

Details of the implementation and performance of the preceding filter are provided in [Fu et al. \(2010\)](#).

#### ATMOSPHERIC FORCING

The surface stress ( $p_s$ ) in Equation (6) can be used to apply a pressure to the interface to generate a known disturbance. The formulation in terms of the gradient of Heaviside function ensures that the stress is applied only at the free surface. The stress is applied for a finite amount of time with an amplitude that is slowly ramped up and down to minimize transients. The surface stress can be used to generate a linear superposition of waves in the following manner:

$$p_s = G(t) \left\{ A_r + \sum_{n=1}^N A_n \cos \left[ k_n(x + U_c t) - \omega_n(t - T_u) \right] \right\}, \quad (12)$$

where  $A_n$ ,  $k_n$ , and  $\omega_n$  are respectively the Fourier amplitude, wavenumber, and frequency. Typically, the wavenumber and wave frequency satisfy a linear dispersion relationship,  $\omega_n^2 = k_n^2 / F_r^2$ .  $U_c$  is the current velocity. In a frame of reference that is fixed with the crest

of the wave,  $U_c$  equals the phase speed ( $\omega_n / k_n$ ).  $T_u$  is an unwinding time that can be used to generate steep events at  $t = T_u$ .  $G(t)$  ramps up and down the stress for  $0 \leq t \leq T_f$ :

$$G(t) = \frac{1}{2} \left[ 1 - \cos \left( \frac{2\pi t}{T_f} \right) \right]. \quad (13)$$

$G(t) = 0$  for  $t > T_f$ . A three-dimensional uniform random disturbance is passed through a low-pass filter and added to the flow. The r.m.s. amplitude of the  $A_r$  integrated over the fluid volume is  $a_o$ :

$$\frac{1}{V} \int_V dV A_r^2(x_i) = a_o^2. \quad (14)$$

#### SIMULATION PARAMETERS

For all the simulations in this study  $L_o = 1/k = 1$ ,  $U_o = (g/k)^{1/2} = 1$ , and  $Fr = 1$ . The length of the domain is  $2\pi$ . The depth of the water and the height of the air are set equal to  $\pi$ , and the width of the domain is  $\pi/2$ , as illustrated in Figure 1. Coarse, medium, and fine NFA simulations are performed with respectively  $256 \times 64 \times 256$ ,  $512 \times 128 \times 256$ , and  $1024 \times 256 \times 512$  grid points.

For the finest resolution cases, the time step  $\Delta t = 0.002$  for  $t \leq 9$  when the wave is developing, and  $\Delta t = 0.001$  for  $t > 9$  when the wave is breaking. Density-weighted velocity smoothing is applied every 20 time steps using simple averaging over  $3 \times 3 \times 3$  grid cells. The finest resolution simulations are run up to  $t = 36.5$ , corresponding to 32,000 time steps.

The pressure forcing that is used in these simulations consists of four values of  $A_o / (2\pi) = 0.017, 0.018, 0.019, 0.020$  corresponding to initial overturning events characterized by weak plunging (WP), plunging (P), strong plunging (SP) and very strong plunging (VSP). Each breaking-wave amplitude is simulated using coarse (C), medium (M), and fine (F) resolution. Cases discussed in the results section will be referred to by the type of breaking and grid resolution. For example,  $VSP^F$  would refer to a very strong plunging simulation at the fine grid resolution. The other parameters in the atmospheric forcing are  $U_c = -1$ ,  $k_o = 1$ ,  $\omega_c = 1$ ,  $T_u = 0$ ,  $T_f = 4\pi$ , and  $a_o = 0.1A_0$ .

#### VALIDATION

A comparison to a Boundary Integral Equation Method (BIEM) [Dommermuth et al. \(1988\)](#) is presented to show that the aforementioned atmospheric pressure forcing technique generates fully non-linear progressive waves. Cuts of the free-surface at  $y = 0$  from cases  $VSP^C$ ,  $VSP^M$ , and  $VSP^F$ , which are the coarse, medium and fine resolution cases corresponding to a very

Case	Resolution	$\frac{ \int dV(\phi - \phi_0) }{\int dV \phi_0}$
Very Strong Plunging	Coarse	$2.10E^{-4}$
·	Medium	$3.14E^{-4}$
·	Fine	$3.31E^{-4}$
Strong Plunging	Coarse	$1.59E^{-4}$
·	Medium	$2.61E^{-4}$
·	Fine	$2.22E^{-4}$
Plunging	Coarse	$1.37E^{-4}$
·	Medium	$1.91E^{-4}$
·	Fine	$5.16E^{-5}$
Weak Plunging	Coarse	$1.32E^{-4}$
·	Medium	$1.08E^{-4}$
·	Fine	$6.35E^{-4}$

Table 1 Mass conservation over total duration of simulation.

strong plunging event ( $A_o/2\pi = 0.02$ ), are compared. In addition coarse, medium and fine BIEM simulations are performed with respectively 512, 1024, and 2048 nodes along the free surface. Figure 2(a) compares the finest resolution NFA and BIEM simulations. The slight difference between NFA and BIEM in the tip of the plunging breaking wave may be due to the effects of air in the NFA simulations. Figure 2(b) and Figure 2(c) show grid studies of three-dimensional NFA simulations and two-dimensional BIEM simulations, respectively. The three-dimensional NFA simulations, which have less grid resolution than the two-dimensional BIEM simulations, resolve the plunging jet better than the BIEM simulations. Table 1 shows that mass is conserved over the duration of the simulation. The method proposed here including the smoothing and projection operation is mass conservative.

Having shown agreement with BIEM methods up to reentry, attention is now focused on the flow after reentry.

### Flow Visualizations

Figure 3 shows the free surface visualized with the 50% iso contour of the volume fraction at eight times for each of the plunging breaking cases. Columns A-D show results from cases  $VSP^F$ ,  $SP^F$ ,  $P^F$ , and  $WP^F$ , respectively. The electronic version of the document has zoomable images which enables the reader to enlarge a panel of Figure 3 to the full window size by clicking it. Each of the frames has been selected to correspond to the following stages in the breaking cycle:

- 1. Vertical Front Face:** The wave becomes asymmetric with the front face becoming vertical, and the the tip begins to form.
- 2. Pinch Off:** The tip of the plunging breaker touches down on the surface below, causing an ovular cavity of air to be pinched off.
- 3. Splash-up:** The touch down of the jet formed in the

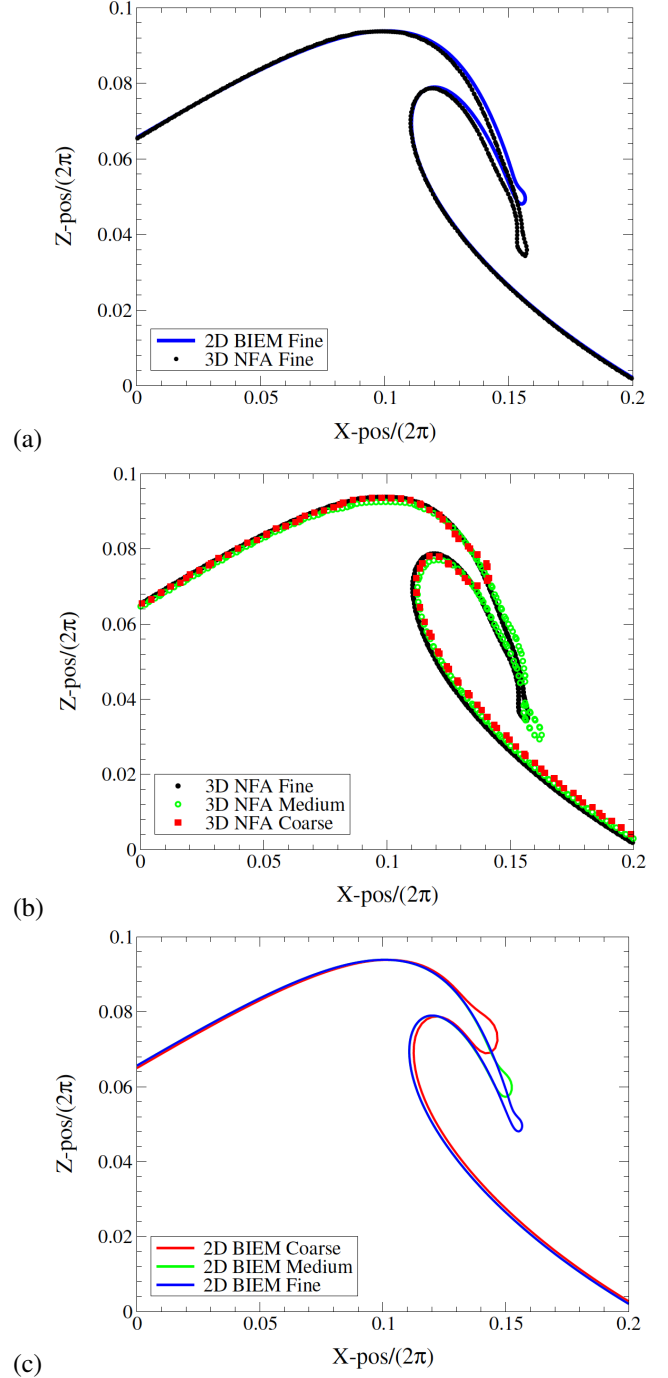


**Figure 2:** (a) Comparison of fine resolution 3-D NFA simulations to the fine resolution 2-D BIEM calculations just before reentry. (b) Comparison of three-dimensional NFA simulations at different grid resolutions just before reentry. (c) Comparison of two-dimensional BIEM simulations at different grid resolutions just before reentry.



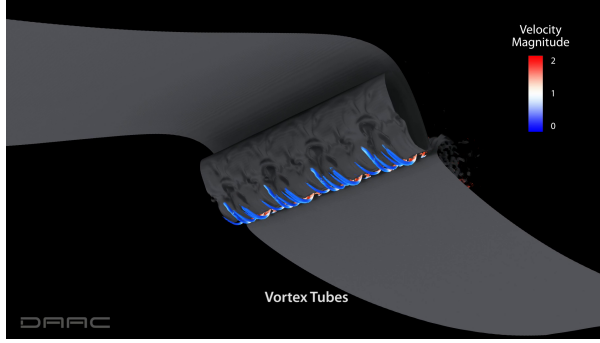


**Figure 4:** Vortex tubes apparent on back of ovular cavity of air for case  $VSP^F$

pinch-off stage forces up a secondary jet. Since, the jet in the pinch-off stage impacts the surface almost vertically, the splash up is nearly vertical.

**4. Interaction:** The nearly vertical splash-up, which may reach a height greater than the wave crest, interacts with the advancing wave crest and causes the entrained air cavity to tilt. This three-way interaction allows the cavity to reconnect with the free-surface. This reconnection provides an escape path for the air.

**5. Tip Break Off:** The advancing wave crest is now past the splash-up region and carries the splash-up region beneath the crest with the wave. The portion of the splash up that reached a height greater than the wave crest is either whipped forward or broken off.

**6. Tip Impact:** The portion of the splash up above the wave crest that remains attached is slammed down onto the front face, and the portion of splash up that broke free crashes into the front face.

**7. Dual Breaking:** Forward and backward plunging events are evident, giving the wave a mushroom top look. It is the time at which the large bubble cloud is formed and entrainment occurs at both the forward and rear plunging locations.

**8. Spilling:** A sequence of weaker and weaker plunging and spilling events occur on the front face until a steady progressive wave is formed.

In addition to the contours of the volume fraction, contours of the vorticity and velocity magnitude show interesting three-dimensional structures. Figure 4 shows the magnitude of the velocity overlaid on the free surface for case  $VSP^F$  at  $t = 14.7$ . Evidence of vortex tubes, and hairpin like structure are evident on the back of the initial cavity of air entrained by the primary plunging event. Similar structures have been observed in high definition video of the large waves breaking on beaches (Walker, 2009).

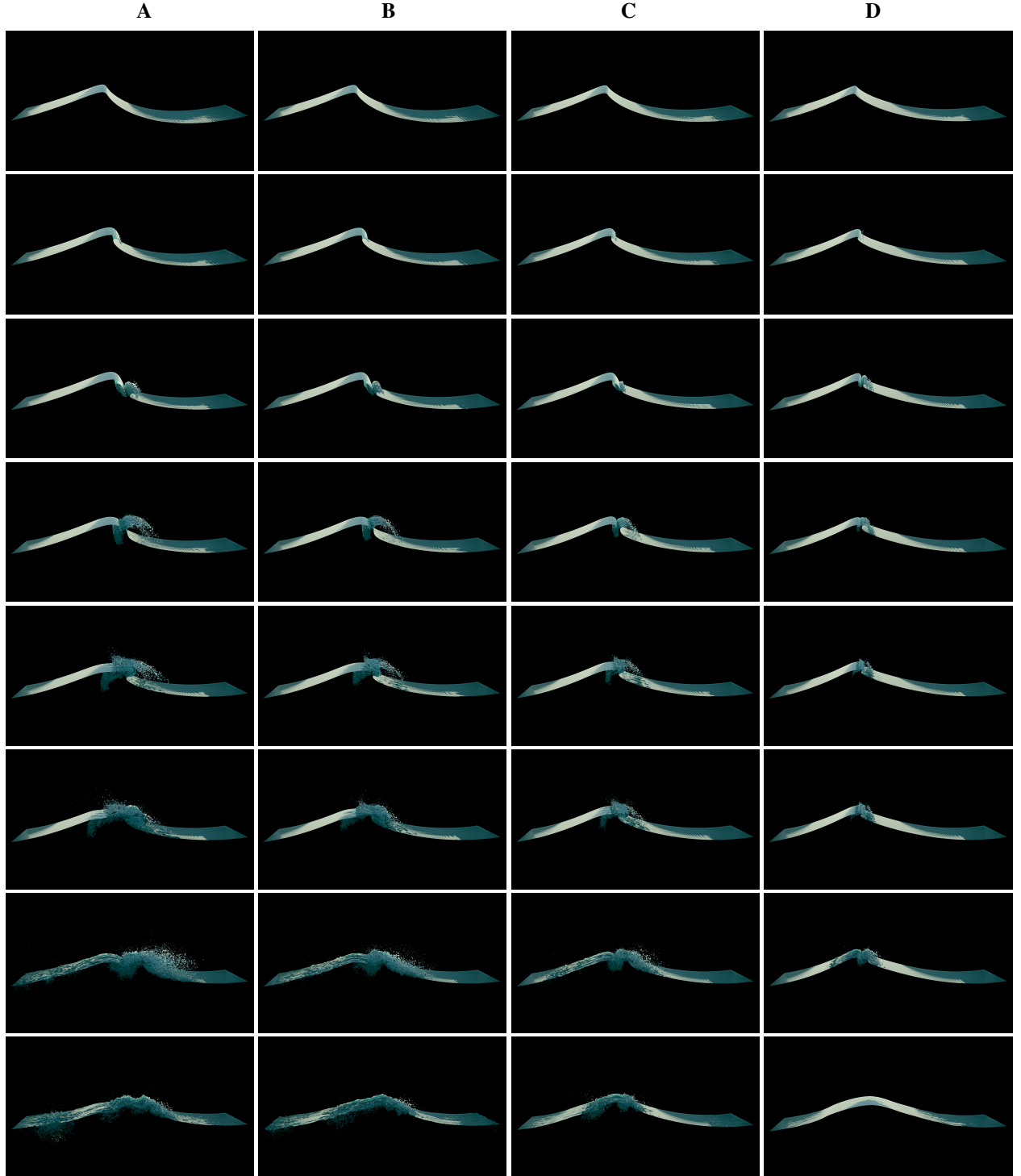
## Volume Integrated Energetics and Air Entrainment

Figure (5) is a plot the the total energy,

$$E(t) = \int_V dV \left( \frac{\rho(t)}{2} u_i(t) u_i(t) + \frac{[\rho(t) - \rho(0)] z}{F_r^2} \right), \quad (15)$$

over time. Four distinct stages are evident in Figure 5, including: (A) Atmospheric forcing; (B) Potential flow before breaking; (C) Breaking which consists of plunging, spilling and splash-up events; and (D) Potential flow after breaking. Note the unequal length of stages B, C, and D, shown at the top of Figure 5. Figure 5 also illustrates the grid resolution necessary to correctly resolve strong plunging events. The minimum resolution is on the order of 1000 grid points per wave length. Stage C is the most interesting as it is characterized by turbulent motions, air entrainment (bubbles), and droplet formation, which leads to complex interactions between the kinetic and potential energies. The VSP and SP cases lose over half their total energies due to the effects of breaking. Figure 6 shows the total amount of air that is entrained per unit width for finest resolution breaking-wave studies. By our definition, the amount of air that is entrained is based on how much air is surrounded by the outermost 50% iso contour of the volume fraction. Based on this definition, there will always be small amounts of entrained air as is evident for  $t < 14$ . The first entraining events are due to the tip of the plunging breaking wave closing off an air cavity. For VSP, SP, P, and WP-type breaking, this occurs at  $t \approx 14$ ,  $t \approx 14.5$ ,  $t \approx 15$ , and  $t \approx 16.5$ , respectively. The first entraining event is followed by sudden dip when the 50% iso contour opens up to the air due to the violent impact of the jet. Slightly later entraining events are due to splash ups, especially for the VSP ( $16 < t < 25$ ) and SP ( $16 < t < 25$ ) cases. During these splash-up events, the amount of entrained air is nearly constant, which indicates that entraining balances degassing through the free surface. After the main splash-ups, air is entrained at the toe of spilling region. During this stage, the air that had been entrained by plunging and splash ups degasses more quickly than air can be entrained by spilling. This occurs for  $t > 25$  for the VSP and SP cases, for  $t > 22$  for the P case, and for  $t > 20$  for the WP case. When viewing Figure 6, it is helpful to refer to Figure 3, which shows three-dimensional views of the wave breaking, and Figures 9-16, which show various energy terms. Similar air entrainment calculations had been performed by Drazen et al. (2010) who have good agreement with laboratory measurements of the void fraction behind a wetted transom.

The maximum air entrained beneath the free surface does not occur at pinch-off. Inspection of Figure 6(a) shows that it occurs well after the initial cavity of air is entrained. Figure 6(b) shows that maximum value of air



**Figure 3:** Three-Dimensional renderings of the 50% iso-contour of the volume fraction. Cases  $VSP^F$ ,  $SP^F$ ,  $P^F$ , and  $WP^F$  are shown in columns A, B, C and D respectively. The frames here correspond to those in Figures 9-10, 11-12, 13-14, and 15-16, respectively. Note: the electronic version of this document contains high resolution frames that can be zoomed in on by clicking the desired frame.

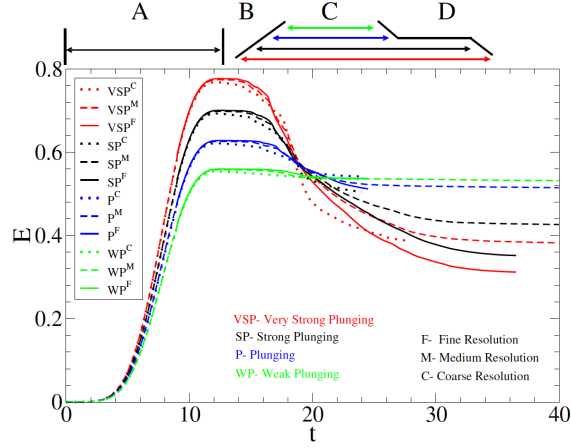


**Figure 5:** Volume integrated energy: potential plus kinetic (see Equation 15).

entrained as a function of the pinch off height,  $h$ . That is the difference in elevation between the crest and the point at which the toe impacts the front face (Drazin et al., 2008). The maximum air entrained per unit width is a linear function of the pinch-off height.

Figure 7(a)-(d) shows the rate of change of the total energy per unit width for cases  $VSP^F$ ,  $SP^F$ ,  $P^F$ , and  $WP^F$ , respectively. Each figure has 8 points labeled which correspond to distinct changes in the rate of change of the total energy. Inspection of Figure 6(b) shows that the volume of air beneath the free surface changes dramatically at the same times that the large changes in the dissipation rate are observed. The next section develops a statistical framework in which to analyze immiscible multi-phase flows, which is then applied to the breaking waves simulated here to further analyze the mechanisms which are responsible for air entrainment and changes in the dissipation rate.

### Statistical Energy Analysis of Multiphase Flows

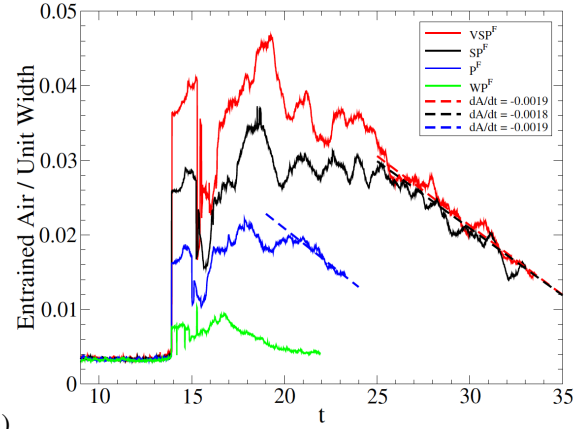
In the subsequent discussion, angle brackets and single primes are used to denote mean and fluctuating volume-weighted (Reynolds) values, viz.,

$$u_i = \langle u_i \rangle + u'_i. \quad (16)$$

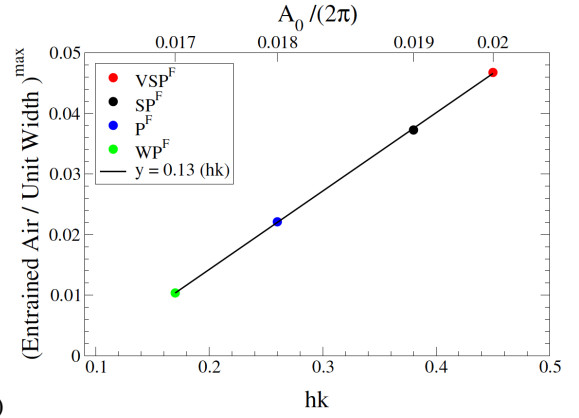
While a tilde and double primes denote mean and fluctuating mass-weighted (Favre) values, viz.,

$$u_i = \tilde{u}_i + u''_i \quad (17)$$

where  $\tilde{u}_i = \langle \rho u_i \rangle / \langle \rho \rangle$ . Here it is noted that the mean mass-weighted velocity is the sum of the Reynolds mean plus the normalized mass flux,  $\tilde{u}_i = \langle u_i \rangle + \langle \rho' u'_i \rangle / \langle \rho \rangle$ .



(a)



(b)

**Figure 6:** Air beneath free-surface, defined by the 50% iso contour of the volume fraction, for cases  $VSP^F$ ,  $SP^F$ ,  $P^F$ ,  $WP^F$ . (a) Air entrained as a function of time. (b) Maximum air entrained as a function of normalized pinch-off height  $kh$ .

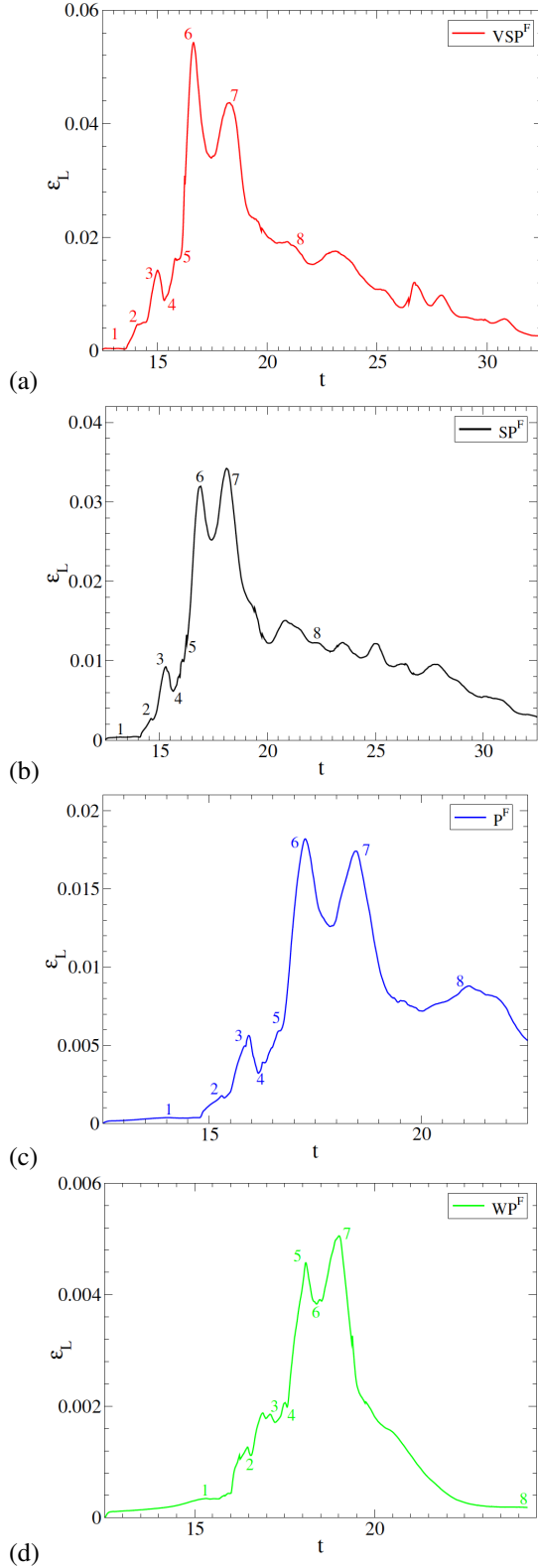


**Figure 7:** Rate of change of Total Energy per unit width shown. (a)  $VSP^F$ , (b)  $SP^F$ , (c)  $P^F$ , (d)  $WP^F$ . Points 1-7 correspond to the rows of Figures 9-10, 11-12, 13-14, and 15-16, respectively.

## MEAN AND TURBULENT KINETIC ENERGY

The total kinetic energy at location  $x_i$  and time  $t$  is:

$$KE \equiv \frac{1}{2} \rho(x_i, t) u_i(x_i, t) u_i(x_i, t). \quad (18)$$

If the kinetic energy is volume averaged then the mean and fluctuating components are:

$$m.k.e. \equiv \frac{1}{2} \langle \rho \rangle \langle u_i \rangle \langle u_i \rangle, \quad (19)$$

and

$$t.k.e. \equiv \frac{1}{2} \langle \rho \rangle \langle u'_i u'_i \rangle + \langle u_i \rangle \langle \rho' u'_i \rangle + \frac{1}{2} \langle \rho' u'_i u'_i \rangle. \quad (20)$$

If the kinetic energy is mass averaged, then the mean and fluctuating components are:

$$m.k.e. \equiv \frac{1}{2} \langle \rho \rangle \tilde{u}_i \tilde{u}_i = \frac{1}{2} \langle \rho \rangle \langle u_i \rangle \langle u_i \rangle + \langle u_i \rangle \langle \rho' u'_i \rangle + \frac{1}{2} \frac{\langle \rho' u'_i \rangle^2}{\langle \rho \rangle}, \quad (21)$$

and

$$t.k.e. \equiv \frac{1}{2} \langle \rho \rangle \langle u'_i u'_i \rangle + \frac{1}{2} \langle \rho' u'_i u'_i \rangle - \frac{1}{2} \frac{\langle \rho' u'_i \rangle^2}{\langle \rho \rangle}. \quad (22)$$

Figure 8(a)-(b) show the m.k.e. and t.k.e. using volume-weighted (Reynolds) and mass-weighted (Favre) averages for case  $VSP^F$  at  $t = 18.5$ . The differences in the m.k.e. are barely discernible, but the t.k.e. shows significant differences. In particular, the t.k.e. based on Reynolds averaging is negative in several regions in the air, whereas the t.k.e. based on Favre averaging is positive everywhere. In addition, the magnitude of the t.k.e. based on Favre averaging is much greater in the water than the air, but the same cannot be said for the Reynolds-averaged t.k.e.. In the subsequent analysis mass-weighted (Favre) averaging is employed.

## MEAN KINETIC ENERGY BALANCE

An evolution equation for the mean kinetic energy can be written as (Chassaing et al., 2002):

$$\left[ \frac{\partial}{\partial t} + \frac{\partial}{\partial x_j} \tilde{u}_j \right] (m.k.e.) = P + B + V - \frac{\partial T_{ik}}{\partial x_k} - \varepsilon, \quad (23)$$

where  $\varepsilon$  is the viscous dissipation rate, which is not modeled here.  $P$  is the shear production of turbulence defined as:

$$P \equiv A_{ik} \frac{\partial \langle \tilde{u}_i \rangle}{\partial x_k}, \quad (24)$$

where

$$A_{ik} = \langle \rho \rangle \langle u'_i u'_k \rangle + \langle \rho' u'_i u'_k \rangle - \frac{\langle \rho' u'_i \rangle \langle \rho' u'_k \rangle}{\langle \rho \rangle}. \quad (25)$$

$B$  is the mean buoyant exchange between kinetic and potential energy, defined as:

$$B \equiv -\frac{\langle \rho \rangle \tilde{u}_3}{Fr^2}. \quad (26)$$

$V$  is the volume expansion work, defined as:

$$V \equiv \langle p \rangle \frac{\partial}{\partial x_k} \left( \frac{\langle \rho' u'_k \rangle}{\langle \rho \rangle} \right), \quad (27)$$

and  $\frac{\partial T_{ik}}{\partial x_k}$  is the transport, defined as:

$$T_{ik} \equiv A_{ik} \tilde{u}_i + \langle p \rangle \tilde{u}_k. \quad (28)$$

Here, attention is returned to Figure 7(a)-(d). Recall that the points labeled 1-8 are the points at which large changes in the dissipation rate are observed. An analysis using the statistical framework developed above is used to garner further insight into the physical processes responsible for the observed changes.

Figures 9, 11, 13, and 15 show the volume fraction, mean kinetic energy, and turbulent kinetic energy for cases  $VSP^F$ ,  $SP^F$ ,  $P^F$ , and  $WP^F$ , respectively. Figures 10, 12, 14, and 16 show buoyant flux, turbulent kinetic energy production due to shear, and volume expansion work for the same cases. All quantities are based on span-wise Favre averaging. Each row is labeled and corresponds to the points labeled in Figures 7(a)-(d).

Recall in the discussion of Figure 3 eight stages were discussed and in each of the subsequent figures the rows correspond respectively to these stages: 1. Vertical Front Face; 2. Pinch Off; 3. Splash-up; 4. Interaction; 5. Tip Break Off; 6. Tip Impact; 7. Dual Breaking; 8. Spilling.

In column C of Figures 9, 11, 13, and 15 turbulent kinetic energy is greatest on the front face of the wave in the toe region of splashing events (row 6). Column B of Figures 10, 12, 14, and 16 show that production of turbulent kinetic energy is also greatest in this region. Based on column A of Figures 9, 11, 13, and 15, there are three types of air entraining events: (1) Breakup of the cavity formed by the first plunging event; (2) Breakup of the cavity formed by the splash-up event; and (3) Entrainment at the toe of the spilling breaking. Plumes of air are periodically entrained and left behind. The greatest amount of air is entrained by the VSP and SP plunging breakers. The depth of the of air entrainment is proportional to the wave amplitude. Based on column A of Figures 9, 11, 13, and 15, the mean kinetic energy is highest in the crest of the first plunging and splashing events. At later time, turbulent kinetic energy is transformed into mean kinetic energy beneath the crest of the

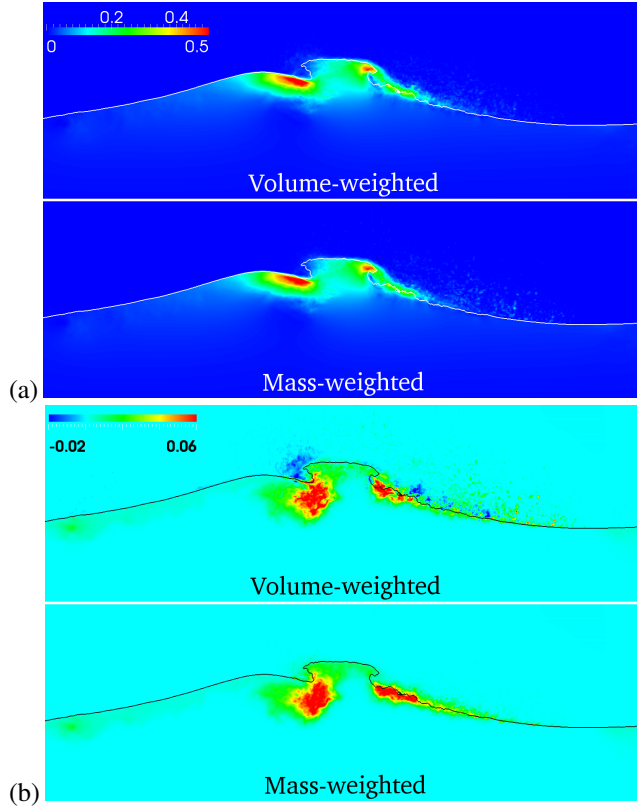


**Figure 8:** Difference in (a) m.k.e. and (b) t.k.e. using volume-weighted averages Eqs. 19-20 and mass-weighted averages Eqs. 21-22, for case  $VSP^F$  at  $t=18.50$ .



spilling breaking region. Based on column A of Figures 10, 12, 14, and 16, the buoyant flux is positive on the front face of waves and negative on the back faces, as expected. The structure of the buoyant flux indicates that energy is being transferred from the primary gravity wave to shorter waves on the front face of the primary gravity wave. The volume expansion work in column C of Figures 10, 12, 14, and 16 is less organized than the production of turbulent kinetic energy, but it too is greatest in the splashing region.

Stage 7 is the stage in which forward and backward plunging events are evident. Significant t.k.e. is generated at both the forward and rear plunging locations. Note that the m.k.e., t.k.e., air entrainment, production, and volume expansion are all larger at the rear breaking region. It is also the region in which the large bubble cloud is formed. The buoyancy sets up a rear recirculation zone, which pumps air down. In Figure 11(A7) notice the rear breaking region has a positive B region beneath the negative region which causes the water to push up on the free-surface and provide a path way for air to be driven into.

It is after this stage that the distinct deep and shallow air volumes are evident in Figures 9(A8), 11(A8) and 13(A8). The presence of the deep and shallow bubble clouds has been observed in the experiments of Rapp and Melville (1990) and are discussed in the review of Melville (1996).

## Computational Improvements

The Numerical Flow Analysis (NFA) code was originally designed to provide turnkey capabilities to model the flow around breaking waves around ship hulls, including plunging and spilling breaking waves, the formation of spray, and the entrainment of air (see Dommermuth et al., 2007; O'Shea et al., 2008). In the most recent development cycle the types of problems for which it is well suited have been significantly extended. To provide some perspective to the scope of problems NFA can accurately simulate, consider that there are five other symposium papers based, all or in part, on NFA simulations, including: (1) Numerical predictions of seaway by Dommermuth et al. (2010); (2) Comparisons of model-scale experimental measurements and computational predictions for the transom wave of a large-scale transom model by Drazen et al. (2010); (3) Parameterization of the internal-wave field generated by a submarine and its turbulent wake in a uniformly stratified fluid by Rottman et al. (2010); (4) A comparison of measured and predicted wave impact pressures from breaking and non-breaking waves by Fullerton et al. (2010); and (5) A comparison of experimental measurements and computational predictions of a deep-V planing hull by Fu et al. (2010).

In addition to the advances in the numerical methods which expanded the capabilities, one significant modification to the inter-processor data communication routines and sub-domain layout has been implemented. This modification leverages the small number of blocks (or sub-domains) in any one direction that result from the three-dimensional domain decomposition and allows 1-dimensional sub-communicators to replace the global communicator in MPI collective data operations. The modifications to the data-communication improve the execution time in terms of wall-clock hours and CPU hours required per unknown by a factor of 2 or more. More importantly the elimination of the collective data operations allows NFA to scale to thousands of processors.

To demonstrate the ability of NFA to scale to thousands of processors, a weak scaling analysis is performed. Weak scaling, in the context of high performance computing, is a measure of how an algorithm performs when the problem size per node is held constant and the number of nodes is increased. In this type of analysis as the number of cores increases, the number of unknowns increases in direct proportion. Here the problem size is  $128^3$  unknowns per node and the iterations per hour achieved on 8, 64, 512, and 1024 nodes is timed. To add perspective as to total number of unknowns, the case with 1024 cores has 2.15 billion unknowns and the case with 8 cores has 16.7 million unknowns. The analysis has been carried out on the the SGI Altix ICE cluster (Diamond located at the ERDC). The results are shown in Figure 17, along with the predicted performance on the new Cray XT6 platforms. In summary, Figure 17 shows that in its current form NFA can efficiently simulate jobs with 2+ billion unknowns in a reasonable number of wall-clock hours.

The scalings in Figure 17 are based on normal working conditions with many users running jobs. On a dedicated machine, the node layout can be optimized leading to an additional factor of two increase in performance. Recent simulations on the SGI ALTIX ICE platform, discussed in Drazen et al. (2010), achieved nearly 340 iteration per hour with 1.05 billion unknowns. Assuming that the speed of the new Cray XT6 is twice that of the SGI ALTIX and that dedicated access time is available, a factor of four speed increase can be expected. It is reasonable to assume that in this environment 10 billion cell jobs can achieve 100 iterations/hour.

## Conclusions

The formulation for a canonical deep-water breaking wave is developed. In conjunction, an atmospheric pressure forcing technique which is able to generate fully non-linear progressive waves is developed and validated. Together they enabled a systematic study of deep-water

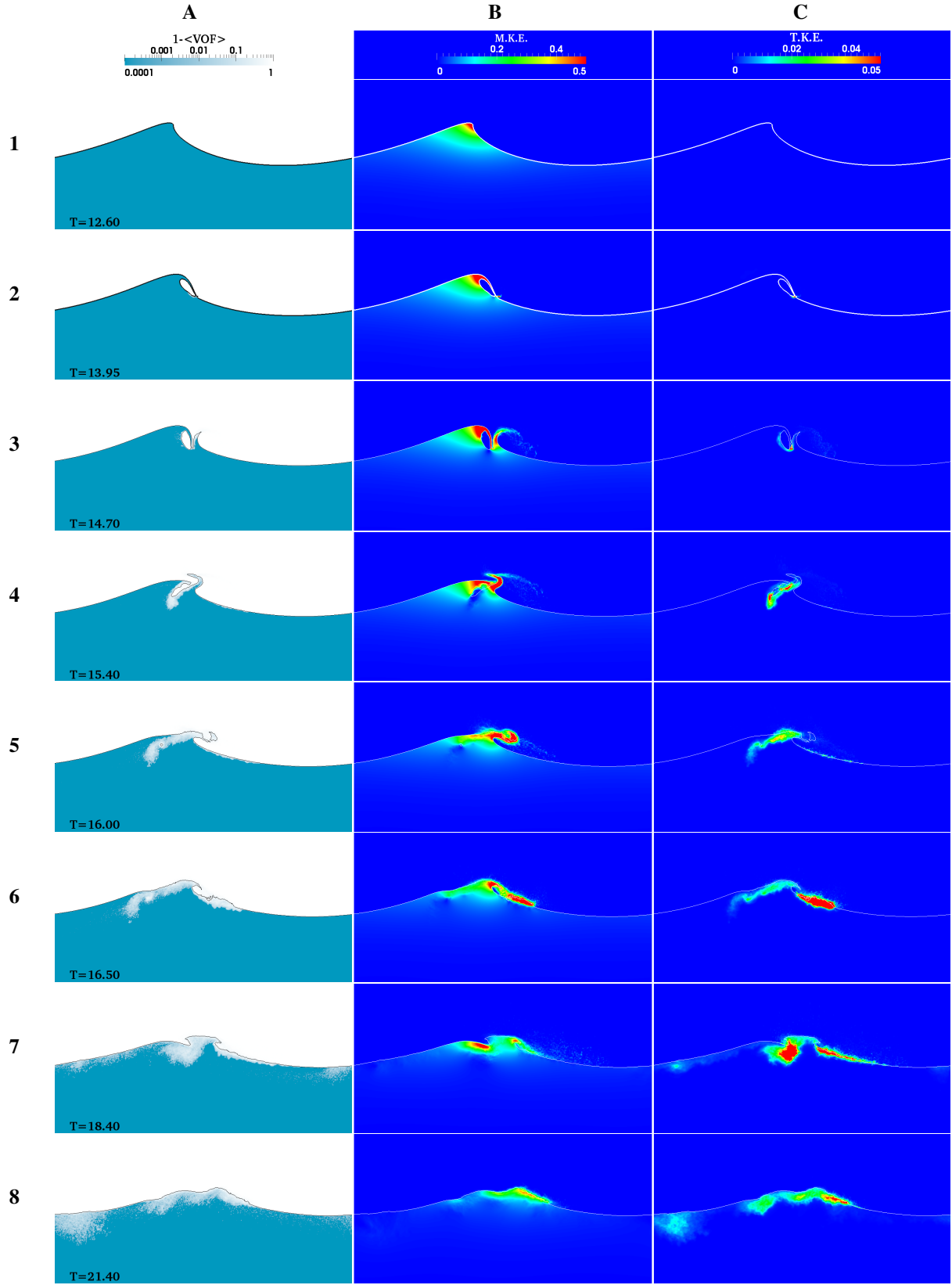


**Figure 9:** Volume of Air, Mean Kinetic Energy (Eq. 21), and Turbulent Kinetic Energy (Eq. 22) for case  $VSP^F$ . The non-dimensional time is given in the lower left corner of column A and the contour levels are given at the top of each column.

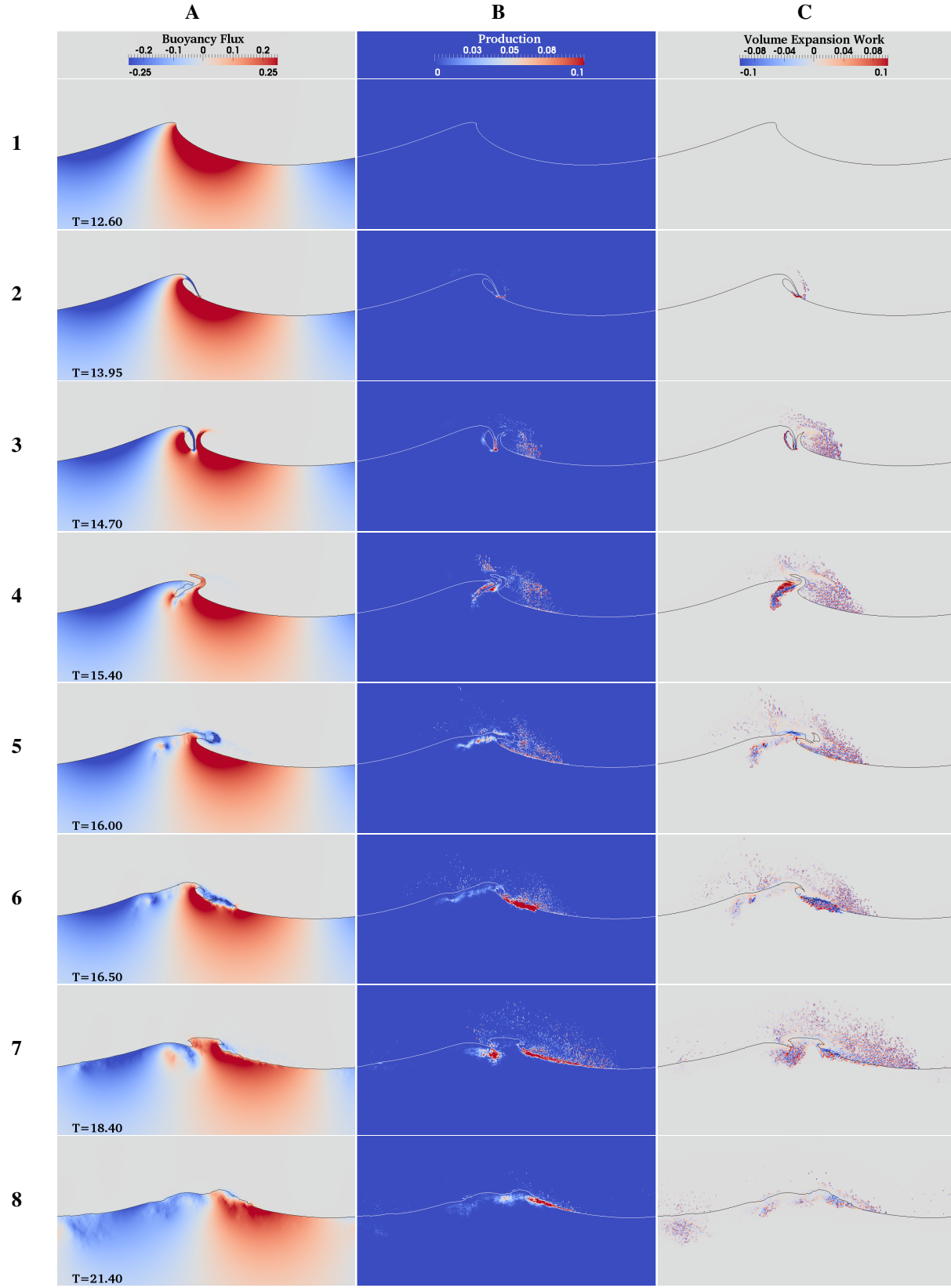


**Figure 10:** Buoyant Flux, Shear Production of T.K.E., Volume Expansion Work for case  $VSP^F$ . The non-dimensional time is given in the lower left corner of column A and the contour levels are given at the top of each column.

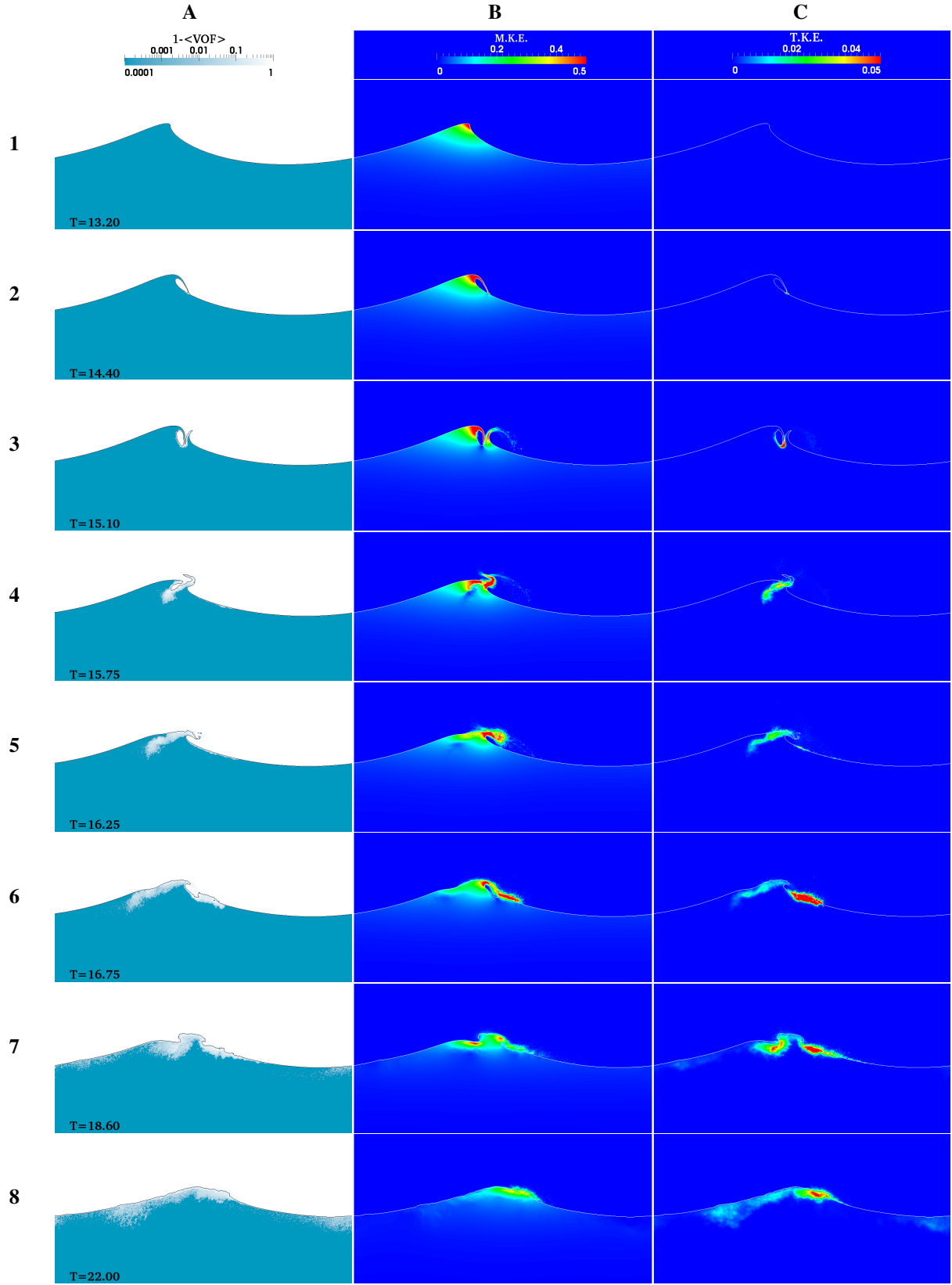


**Figure 11:** Volume of Air, Mean Kinetic Energy (Eq. 21), and Turbulent Kinetic Energy (Eq. 22) for case  $SP^F$ . The non-dimensional time is given in the lower left corner of column A and the contour levels are given at the top of each column.

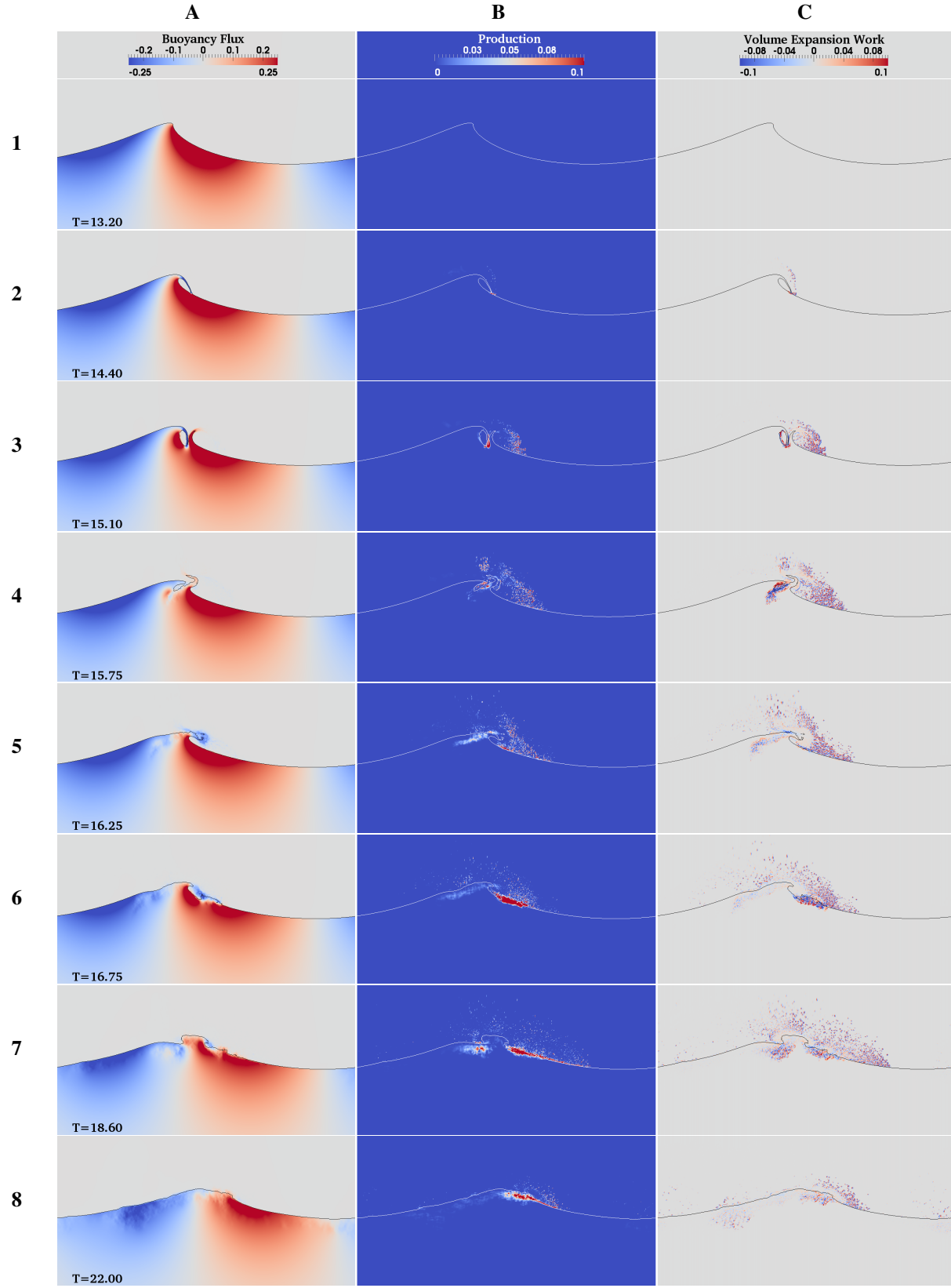


**Figure 12:** Buoyant Flux, Shear Production of T.K.E., Volume Expansion Work for case  $SP^F$ . The non-dimensional time is given in the lower left corner of column A and the contour levels are given at the top of each column.



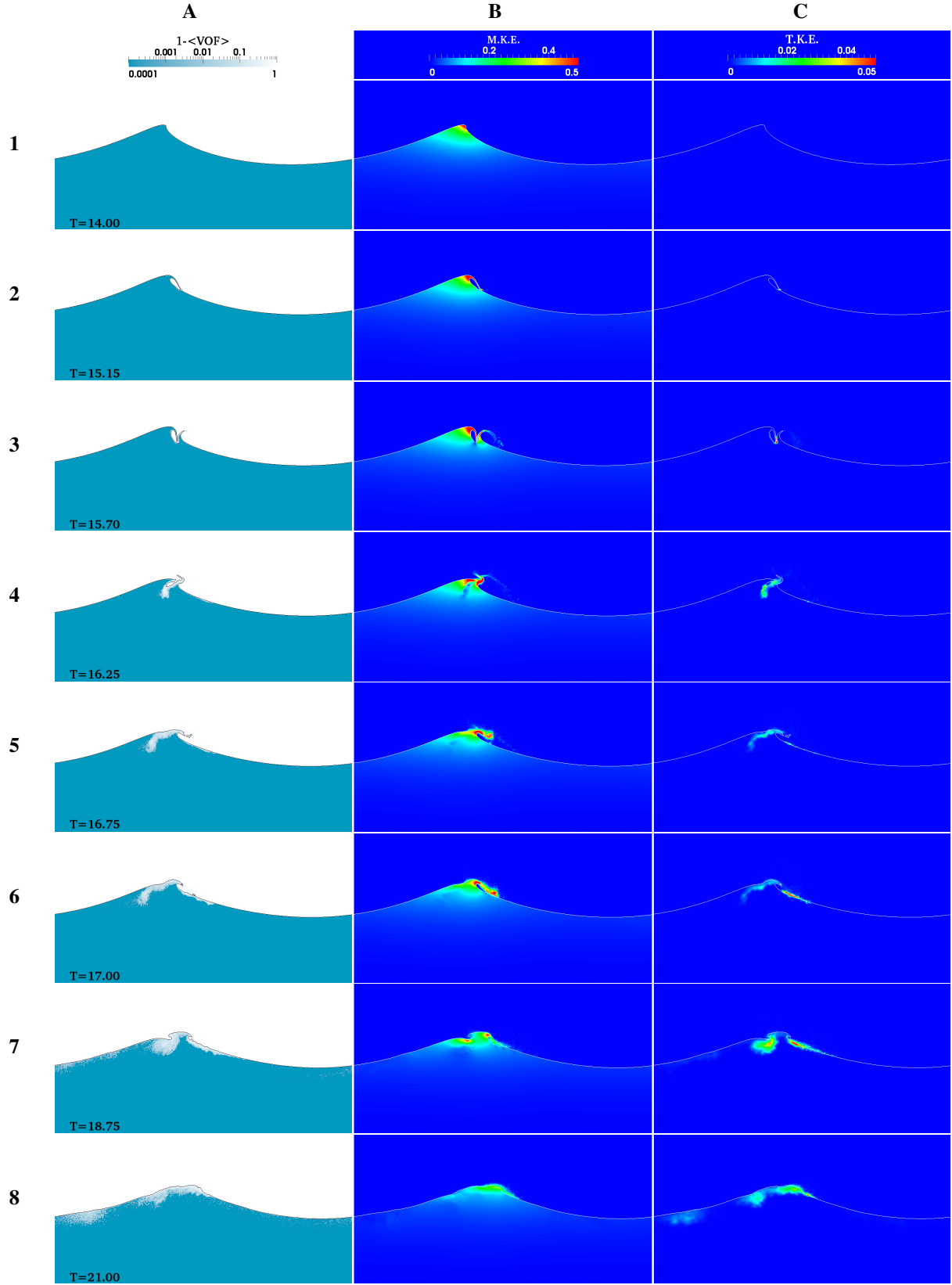


**Figure 13:** Volume of Air, Mean Kinetic Energy (Eq. 21), and Turbulent Kinetic Energy (Eq. 22) for case  $P^F$ . The non-dimensional time is given in the lower left corner of column A and the contour levels are given at the top of each column.

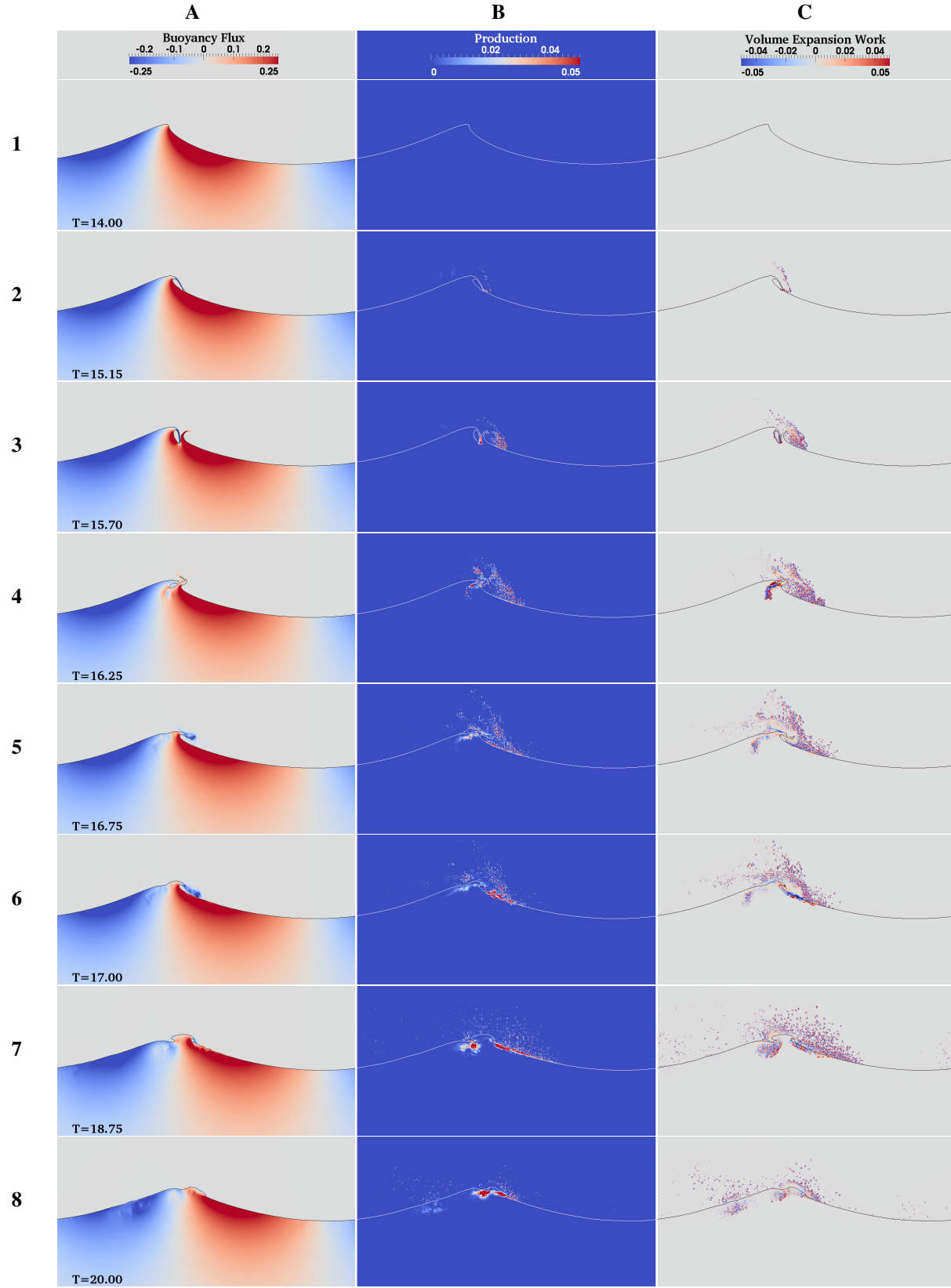


**Figure 14:** Buoyant Flux, Shear Production of T.K.E., Volume Expansion Work for case  $P^F$ . The non-dimensional time is given in the lower left corner of column A and the contour levels are given at the top of each column.

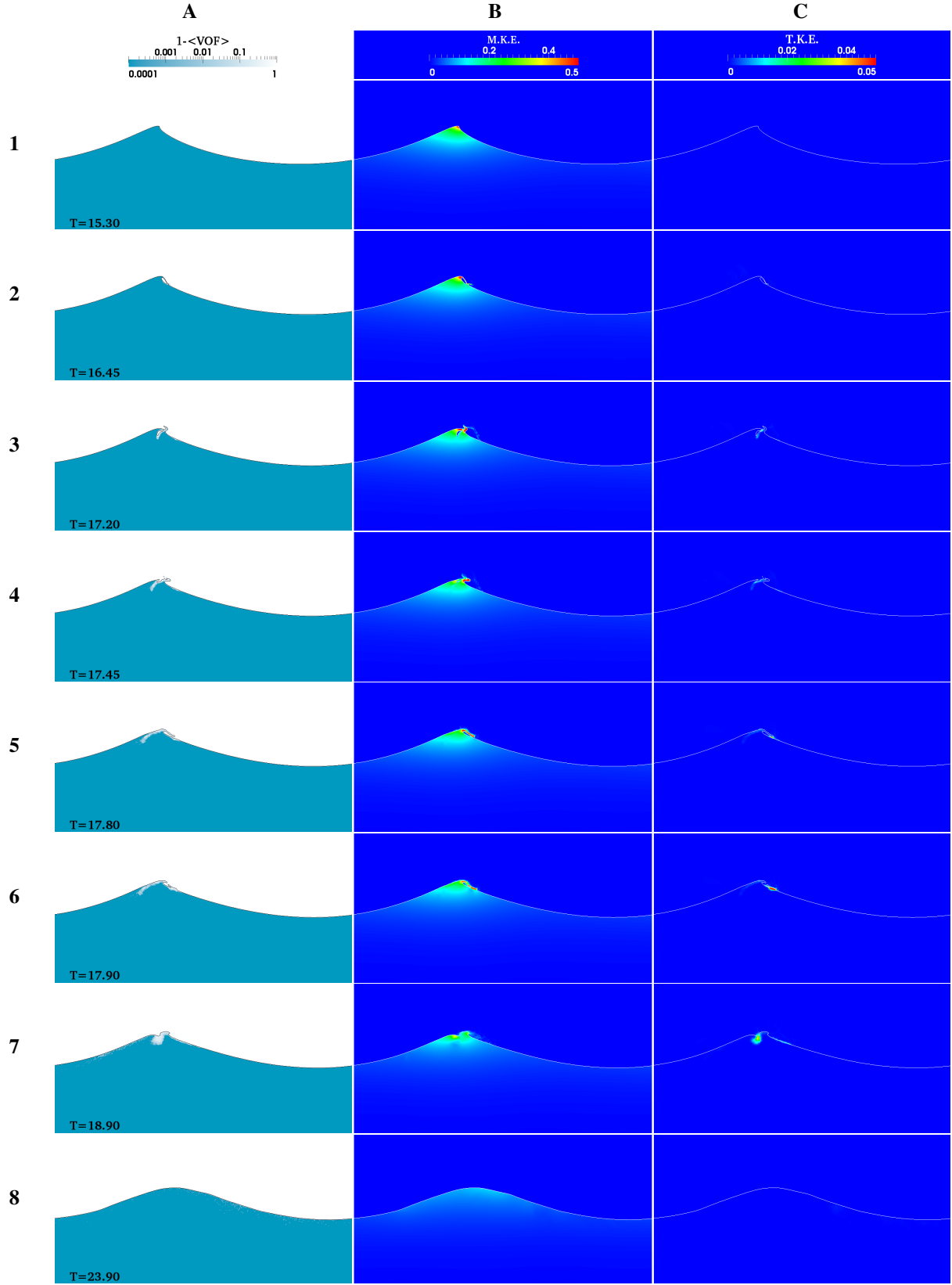


**Figure 15:** Volume of Air, Mean Kinetic Energy (Eq. 21), and Turbulent Kinetic Energy (Eq. 22) for case  $WP^F$ . The non-dimensional time is given in the lower left corner of column A and the contour levels are given at the top of each column.

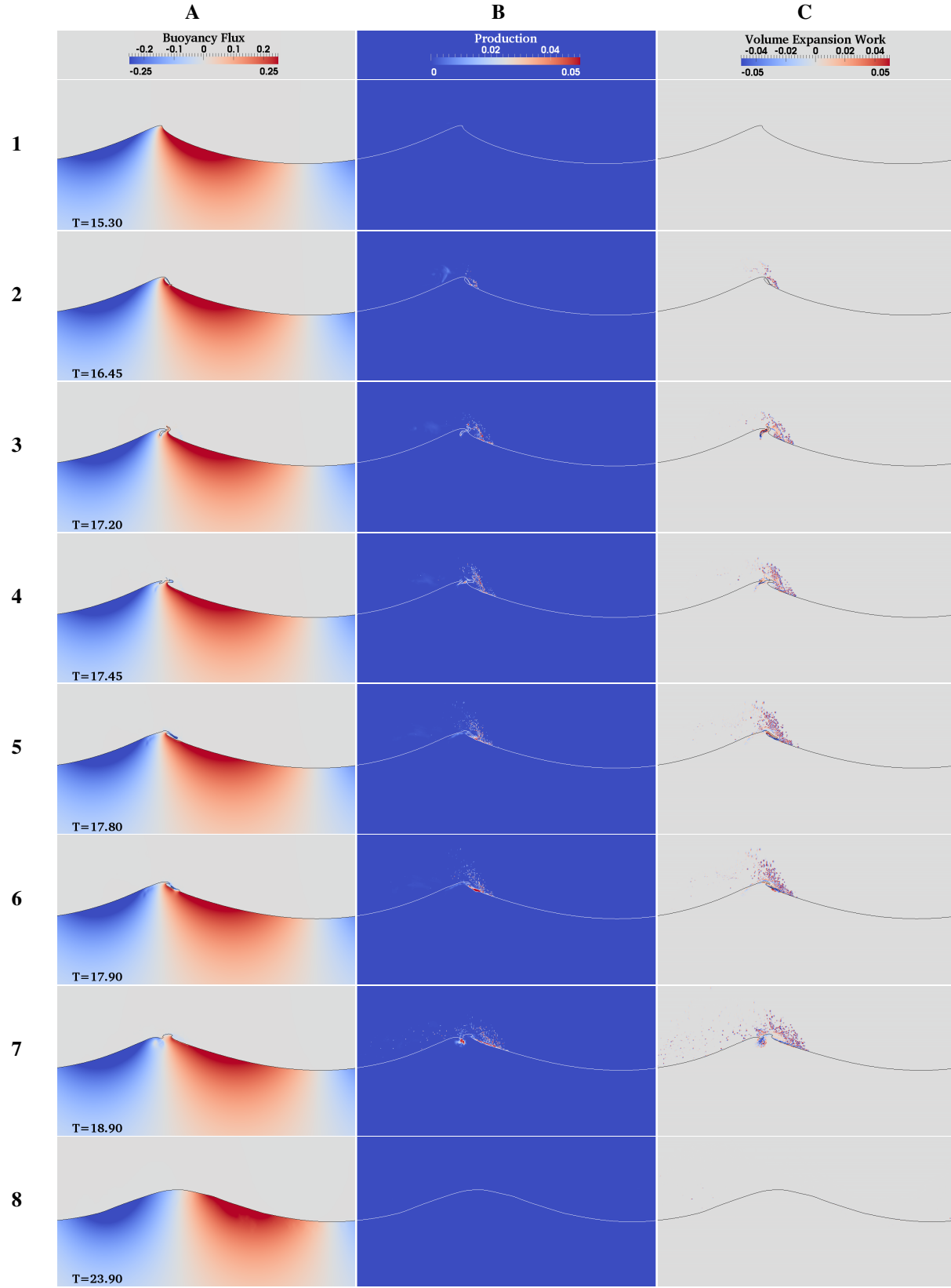


**Figure 16:** Buoyant Flux, Shear Production of T.K.E., Volume Expansion Work for case  $WP^F$ . The non-dimensional time is given in the lower left corner of column A and the contour levels are given at the top of each column.

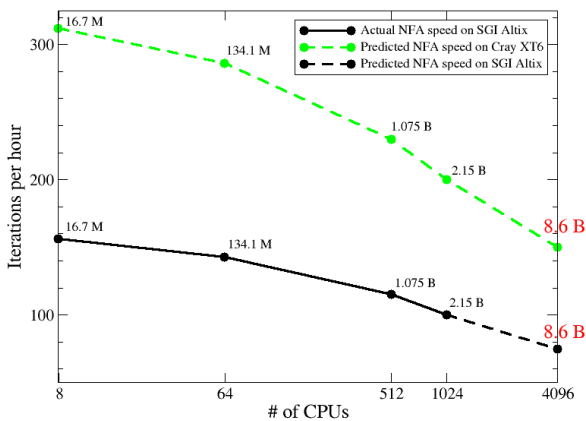


**Figure 17:** The number of iterations (time steps) per hour achieved while the number of grid points (unknowns) per core is fixed at  $128 \times 128 \times 128$  and the number of CPU's (or cores) is increased.

plunging breaking waves.

## Acknowledgments

The Office of Naval Research supports this research. Dr. Patrick Purtell is the program manager. This work is supported in part by a grant of computer time from the [DOD High Performance Computing Modernization Program](#). The numerical simulations have been performed on the Cray XT4 at the U.S. Army Engineering Research and Development Center (ERDC). Animations of the breaking wave simulations are available at <http://www.youtube.com/waveanimations>.

## References

- Chassaing, P., Antonia, R., Anselmet, F., Joly, L., and Sarkar, S., *Variable Density Fluid Turbulence*, Kluwer Academic Publishers, Dordrecht, The Netherlands, 2002.
- Dommermuth, D. G., Fu, T. C., O'Shea, T. T., Brucker, K. A., and Wyatt, D. C., "Numerical prediction of a seaway," *Proceedings of the 28th Symposium on Naval Hydrodynamics*, Pasadena, California, USA, 2010, to appear.
- Dommermuth, D. G., O'Shea, T. T., Wyatt, D. C., Ratcliffe, T., Weymouth, G. D., Hendrikson, K. L., Yue, D. K., Sussman, M., Adams, P., and Valenciano, M., "An application of cartesian-grid and volume-of-fluid methods to numerical ship hydrodynamics," *Proceedings of the 9th International Conference on Numerical Ship Hydrodynamics*, Ann Arbor, Michigan, 2007.
- Dommermuth, D. G., Yue, D. K., Lin, W.-M., Rapp, R., Chan, E., and Melville, W., "Deep-water plunging breakers: a comparison between potential theory and experiments," *J. Fluid Mech.*, Vol. 189, 1988, pp. 423–442.
- Drazen, D. A., Fullerton, A. M., Fu, T. C., Beale, K. L., O'Shea, T. T., Brucker, K. A., Wyatt, D. C., Bhushan, S., Carrica, P. M., and Stern, F., "Comparisons of model-scale experimental measurements and computational predictions for the transom wave of a large-scale transom model," *Proceedings of the 28th Symposium on Naval Hydrodynamics*, Pasadena, California, USA, 2010, to appear.
- Drazin, D., Melville, W., and Lenain, L., "inertial scaling of dissipation in unsteady breaking waves," *Journal of Fluid Mechanics*, Vol. 611, 2008, pp. 307–332.
- Duncan, J., "Spilling breakers," *Annual Review of Fluid Mechanics*, Vol. 33, 2001, pp. 519–547.
- Fu, T. C., Ratcliffe, T., O'Shea, T. T., Brucker, K. A., Graham, R. S., Wyatt, D. C., and Dommermuth, D. G., "A comparison of experimental measurements and computational predictions of a deep-v planing hull," *Proceedings of the 28th Symposium on Naval Hydrodynamics*, Pasadena, California, USA, 2010, to appear.
- Fullerton, A. M., Fu, T. C., Brewton, S., Brucker, K. A., O'Shea, T. T., and Dommermuth, D. G., "A comparison of measured and predicted wave-impact pressures from breaking and non-breaking waves," *Proceedings of the 28th Symposium on Naval Hydrodynamics*, Pasadena, California, USA, 2010, to appear.
- Melville, W., "The role of surface-wave breaking in air-sea interaction," *Annual Review of Fluid Mechanics*, Vol. 28, 1996, pp. 279–321.
- Moin, P. and Kim, J., "Numerical investigation of turbulent channel flow," *Journal of Fluid Mechanics*, Vol. 118, 1982, pp. 341–377.
- Moser, R., Rogers, M., and Ewing, D., "Self-similar time evolving plane wakes," *Journal of Fluid Mechanics*, Vol. 367, 1998, pp. 225–289.
- O'Shea, T. T., Brucker, K. A., Dommermuth, D. G., and Wyatt, D. C., "A numerical formulation for simulating free-surface hydrodynamics," *Proceedings of the 27th Symposium on Naval Hydrodynamics*, Seoul, Korea, 2008.



Rapp, R. and Melville, W., “Laboratory measurements of deep-water breaking waves,” Philosophical Transactions of the Royal Society of London, Vol. 331, 1990, pp. 735–800.

Rogers, M. and Moser, R., “Direct simulation of a self-similar turbulent mixing layer,” Physics of Fluids, Vol. 6, 1994, pp. 903–923.

Rottman, J. W., Brucker, K. A., Dommermuth, D. G., and Broutman, D., “Parameterization of the internal-wave field generated by a submarine and its turbulent wake in a uniformly stratified fluid,” Proceedings of the 28th Symposium on Naval Hydrodynamics, Pasadena, California, USA, 2010, to appear.

Walker, M., “Monster wave gives up its secrets,” , 2009.  
**URL:** [http://news.bbc.co.uk/earth/hi/earth\\_news/newsid\\_8035000/8035593.stm](http://news.bbc.co.uk/earth/hi/earth_news/newsid_8035000/8035593.stm)